Sedimentary Geology 235 (2011) 91–99

Contents lists available at ScienceDirect

Sedimentary Geology

journal homepage: www.elsevier.com/locate/sedgeo

Quantitative analysis of iron oxide concentrations within Aptian–Albian cyclic oceanic red beds in ODP Hole 1049C, North Atlantic

Xiang Li, Xiumian Hu *, Yuanfeng Cai, Zhiyan Han

State Key Laboratory of Mineral Deposits Research, School of Earth Sciences and Engineering, Nanjing University, Nanjing 210093, China

ARTICLE INFO

Article history:
Received 14 June 2009
Received in revised form 9 April 2010
Accepted 25 June 2010
Available online 24 July 2010

Keywords:
Cretaceous oceanic red beds
ODP Hole 1049C
Iron oxides
Aptian–Albian
North Atlantic

ABSTRACT

Aptian–Albian sediments in Core 12X of Hole 1049C (ODP Leg 171B) are characterized by high-frequency cycles that consist of alternating layers of red and green/white clayey chalk, and claystone. The first derivative curves of diffuse reflectance spectra (DRS) for samples of different colors reveal that red (brown and orange) samples show clear peaks corresponding to hematite and goethite. Following treatment using the CBD (citrate-bicarbonate-dithionite) procedure, the red samples lost their red color and corresponding peaks in the first derivative curve, and became greenish or whitish. Therefore, hematite and goethite are the minerals responsible for the reddish change in sample color. However, these minerals behave differently from each other in terms of determining the color of sediment: hematite imparts a red color, whereas goethite imparts a yellow color. Therefore, a change in the proportions of hematite and goethite can cause a change in sediment color from orange to brown. To obtain the absolute contents of iron oxides in these sediments, we performed a quantitative analysis using DRS with multiple linear regression. The results reveal that the Albian brown beds contain 0.13–0.82% hematite (average value, 0.51%) and 0.22–0.81% goethite (average value, 0.58%). The Aptian orange beds contain 0.19–0.46% hematite (average value, 0.35%) and 0.29–0.67% goethite (average value, 0.50%). X-ray diffraction analysis of the Aptian and Albian cycles reveals no clear variations in mineral content with sediment color. It is suggested that hematite and goethite were derived from oxic environments during the period of deposition and early diagenesis. The oxic conditions were probably determined by the low accumulation rate of organic matter and the high content of dissolved oxygen in bottom water.

1. Introduction

The Earth system experienced a greenhouse climate for most of the Cretaceous (Tarduno et al., 1998). The sediments deposited in response to this extreme climate included continental coal-bearing sediment strata in polar regions, tropical carbonate platforms in low-latitude regions, desert deposits in subtropical regions, and widespread organic-rich black shales (Skelton et al., 2003). In contrast to the black shales associated with Oceanic Anoxic Events (OAEs), the deposition of Cretaceous oceanic red beds (CORBs) indicates an oxygen-rich marine environment (Hu et al., 2005; Wang et al., 2005). An increasing number of CORBs have been identified worldwide since they were first described in the literature (Eren and Kadir, 2001; Hu et al., 2006a; Melinte and Jipa, 2005; Neuhuber et al., 2007; Wagreich and Krenmayr, 2005; Wang et al., 2009; Yilmaz, 2008).

With the strong progress of two international geosciences programs (IGCP 463 and 494), the topics of paleoceanography and paleoclimatology of CORBs have received increasing attention in recent years (Hu et al., 2005, 2006b; Wang et al., 2005). Nevertheless, highly cyclic red beds have received less attention than long-duration CORBs. In recent decades, high-frequency cycles consisting of CORBs have been widely recognized in the mid- and low-latitude North Atlantic, South Atlantic, mid- and high-latitude Indian Ocean, and mid-latitude Pacific. Studies of such cycles have become increasingly feasible because of the extensive and improved downhole logging undertaken as part of the Deep Sea Drilling Program (DSDP) and Ocean Drilling Program (ODP) (Chen et al., 2007).

Previous studies of marine sediments have shown that diffuse reflectance spectroscopy can be used to distinguish between hematite, goethite, chlorite, organic matter, illite, and montmorillonite in sediments, being especially sensitive in distinguishing different iron oxides (Balsam and Deaton, 1996; Barranco et al., 1989; Ji et al., 2002). Using this approach, hematite and goethite can be detected at concentrations as low as 0.01% by weight (Deaton and Balsam, 1991). Previous studies have also shown that iron oxides are responsible for the red color of CORBs (Channell et al., 1982; Eren and Kadir, 2001; Hu et al., 2006b); however, there are no studies of absolute iron oxide concentrations in CORBs because of their low contents and the limitations of current detection methods.

* Corresponding author. Tel.: +86 25 83593002; fax: +86 25 83686016.
E-mail addresses: lixiang_503@163.com (X. Li), huxm@nju.edu.cn (X. Hu), Caiyf@nju.edu.cn (Y. Cai), zhiyanhan@163.com (Z. Han).

0037-0738/$ – see front matter © 2010 Elsevier B.V. All rights reserved.
doi:10.1016/j.sedgeo.2010.06.024

In the present study, we used diffuse reflectance spectroscopy to determine the absolute concentrations of hematite and goethite in high-frequency cyclic sediments in Core 12X of ODP Hole 1049C in the North Atlantic, with the aim of gaining a better understanding of the origin of high-frequency cyclic red beds. Based on these results, and combined with quantitative X-ray diffraction (XRD) data and geochemical data, we sought to identify the factors that control the development of high-frequency cyclic red beds.

2. Geological setting

The Blake Nose, located in the western North Atlantic, is a salient upon the eastern margin of the Blake Plateau (Fig. 1). The Blake Plateau is generally <1000 m deep, but drops sharply to water depths of >4000 m at the Blake Escarpment because of erosion of the continental slope. In contrast, the Blake Nose is a gently sloping ramp that reaches a maximum depth of about 2700 m at the Blake Escarpment. The Blake Plateau and Blake Nose both consist of an 8 to 12-km-thick sequence of Jurassic and Lower Cretaceous limestone capped by <1 km of Upper Cretaceous and Cenozoic deposits (Benson et al., 1978).

According to the initial reports of ODP 171B (Norris et al., 1998), the Cretaceous Blake Nose sediments span numerous events of paleoceanographic and biological significance, including the Cretaceous–Paleogene extinction and mid-Cretaceous anoxic events. These events are associated with changes in the Earth's biota, biogeochemical cycling, and oceanographic circulation. ODP Leg 171B drilled five holes along a transect along the Blake Nose in water depths of 1344–2670 m (Fig. 1). Among the five drill holes, Site 1049 (30°8.5370′N, 76°06.7271′W) was located in the greatest water depths (2670 m). According to a compilation of Cretaceous magnetic poles, Site 1049 was located at 23°N during the Cretaceous, in a sedimentary environment of the pelagic slope above the carbonate compensation depth (CCD) (Norris et al., 1998). The Cretaceous sediments encountered in drill core at Site 1049 consist mainly of planktonic foraminifers, quartz, and clasts of limestone, dolomite, chalk, chert, and schist (Klaus et al., 2000). Planktonic and benthic species have glassy shells with preserved surface ornamentation and without infilling calcite, thereby indicating that the sediments are almost unaffected by diagenesis (Erbacher et al., 2001).

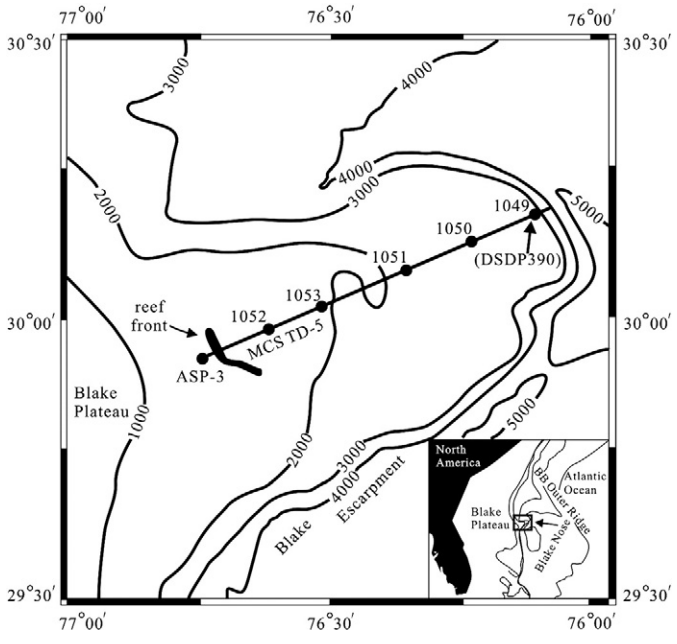

Fig. 1. Bathymetric map of Blake Nose, showing the location of ODP Leg 171B Site 1049 and other sites. Bathymetry is in meters (simplified from Norris et al., 2001).

3. Materials and methods

3.1. Materials

We studied 74 samples from Core 12X of Hole 1049C (Fig. 2), obtained at sampling depths of 139.3–148.1 m below sea floor (mbsf) at a sample interval of 10–15 cm. The sediments are lower Albian to upper Aptian clayey calcareous nannofossil-bearing chalk and claystone rich in planktonic foraminiferal assemblages, with high-frequency variations in color among red (brown/orange), white, and green beds. These rhythmic alternations are interrupted by a 46-cm-thick layer of laminated black shale that correlates with OAE 1b, a black shale sequence known from European sections (Erbacher et al., 2001).

According to Bellier et al. (2000), the planktonic foraminiferal assemblages throughout all of Core 12X are indicative of the *H. planispira* and *H. rischi* zone; however, recent analyses of planktonic foraminifera (B. Huber, Smithsonian Institution, National Museum of Natural History, personal communication) indicate the *P. eubejaouaensis* (replaced the *T. bejaouaensis* as suggested by Premoli-Silva et al., 2009) and *H. rischi* zone, dated to Late Aptian–Early Albian (Fig. 2). Therefore, the age of the core from 139.3 to 148.1 mbsf is Late Aptian–Early Albian, with the Aptian–Albian boundary at 145.3 mbsf.

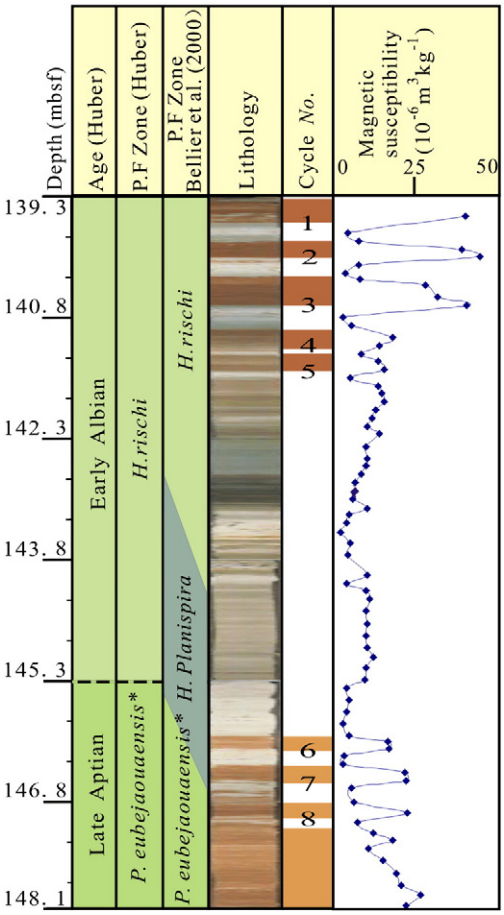

Fig. 2. Integrated stratigraphic log for Core 12X in ODP Hole 1049C, showing sedimentary cycles and magnetic susceptibility (the latter is after Han et al., 2008).* Replaced *T bejaouaensis* Zone by Premoli-Silva et al. (2009).

3.2. Methods

3.2.1. Contents of CBD extractable iron

The red (brown and orange) samples were treated using the CBD (citrate-bicarbonate-dithionite) procedure described by Mehra and Jackson (1960). The contents of CBD extractable iron were determined using a UV-2100 spectrophotometer at the Institute of Surficial Geochemistry at Nanjing University, China. 1 ml of the CBD extractable iron solution was pipetted into a 25 ml colorimetric tube, followed by adding two drops of 1 M hydrochloric acid and 1.25 ml of 2% (mass fraction) ascorbic acid solution. After 20 min of shaking the tube, 2.5 ml of 0.2% (mass fraction) phenanthroline solution and 4 ml of 25% (mass fraction) sodium acetate solution were added into the tube successively, followed by shaking up again. Finally, the solution was diluted to the defined volume of 25 ml with distilled water. Similarly, 6 calibration samples containing 0, 0.1, 0.2, 0.4, 0.8, 1.2 ml of calibration solution (0.1 mg/ml Fe_2O_3) were prepared and diluted to the defined volume of 25 ml. The absorbance of these calibration samples were determined in a 1-cm cell at 510 nm with the UV-2100 spectrophotometer and calculated the regression equation between these absorbances and Fe_2O_3 contents. Subsequently, the absorbance of CBD extractable iron solutions was determined in the same way and calculated the Fe_2O_3 contents of the CBD extractable iron solution by the regression equation.

3.2.2. Quantitative XRD analysis of components

XRD analyses were performed at the State Key Laboratory of Mineral Deposits Research, Nanjing University, China, using a Rigaku D/max IIIa diffractometer equipped with a Cu-target tube and a curved graphite monochromator, operated at 37.5 kV and 20 mA. The slit system was 1° (DS/SS), 0.3 mm RS. Samples were step-scanned with a step size of 0.02° (2θ) from 3° to 100°; the preset time was 2 s/step. XRD samples were prepared using the side-packing method proposed by the National Bureau of Standards (USA). Quantitative analyses of mineral phases and cell parameter refinement were performed by Whole Pattern Fitting using the software Topas (a commercial software of Bruker Corporation). To better illustrate relative changes in terrigenous components with depth in the core, we calculated the mineral content in the non-carbonate fraction, represented by the mineral content in the bulk sample divided by the total mineral content except calcite.

3.2.3. Diffuse reflectance spectroscopy

Samples were analyzed using a Perkin-Elmer Lambda 6 spectrophotometer with a diffuse reflectance attachment, which is capable of measuring sample reflectance from the near-ultraviolet (190–400 nm), visible (400–700 nm), and near-infrared (700–2500 nm) bandwidths, at the Institute of Surficial Geochemistry at Nanjing University, China. Sample preparation and analysis followed the procedures described in Balsam and Deaton (1991) and Ji et al. (2002). Ground samples were made into a slurry on a glass microslide with distilled water, smoothed, and dried slowly at <40 °C. Data are given as percent reflectance relative to the Spectralon™ (reflectance% = 100%). Data processing was restricted to the visible spectrum (400–700 nm), which is the region of the spectrum most sensitive to iron oxide minerals (Deaton and Balsam, 1991). Reflectance data were converted into percent reflectance in standard color bands (Judd and Wyszecki, 1975); i.e., violet = 400–450 nm, blue = 450–490 nm, green = 490–560 nm, yellow = 560–590 nm, orange = 590–630 nm, red = 630–700 nm. These parameters served as independent variables in a transfer function for calculating hematite and goethite content. Percent reflectance in the color bands was determined by dividing the percentage of reflectance in a given color band by the total visible wavelength reflectance in the sample. The total reflectance of each sample, or brightness (Balsam et al., 1999; Ji et al., 2002), was calculated by summing the reflectance values from 400 to 700 nm. Spectral violet, blue, green, yellow, orange, and red were used as independent variables to be related to hematite and goethite concentration via stepwise multiple linear regression. Quantitative measurements of hematite and goethite content followed the method described by Ji et al. (2002), which is summarized in the four steps below.

1) Sample selection
   Previous studies have demonstrated that DRS in the visible region is sensitive to iron oxides. Peaks in first derivative curves have been used to identify the presence of iron oxides, especially hematite and goethite (Deaton and Balsam, 1991). Hematite has a single prominent first derivative peak centered at either 565 or 575 nm, whereas goethite has two first derivative peaks: a primary peak at 535 nm and a secondary peak at 435 nm. In practice, the 435 nm peak is a better indicator of goethite because the 535 nm peak is commonly obscured by hematite (Balsam and Damuth, 2000; Balsam and Wolhart, 1993).Fig. 3a shows the first derivative curves obtained for samples of different color within Core 12X. First derivative curves obtained for brown and orange samples show clear peaks around 435 and 565 nm, corresponding to the goethite and hematite peaks, respectively. These peaks are not observed in any of the other samples; therefore, we selected the orange samples for further analysis based on the following points: (1) there were more orange samples than brown samples, and (2) the orange and brown samples had similar mineralogy.
2) Obtaining matrix materials
   The selected orange samples were treated using the CBD (citrate-bicarbonate-dithionite) procedure (Mehra and Jackson, 1960) two times, to ensure the complete removal of iron oxides. The resulting residues were taken to represent matrix materials from

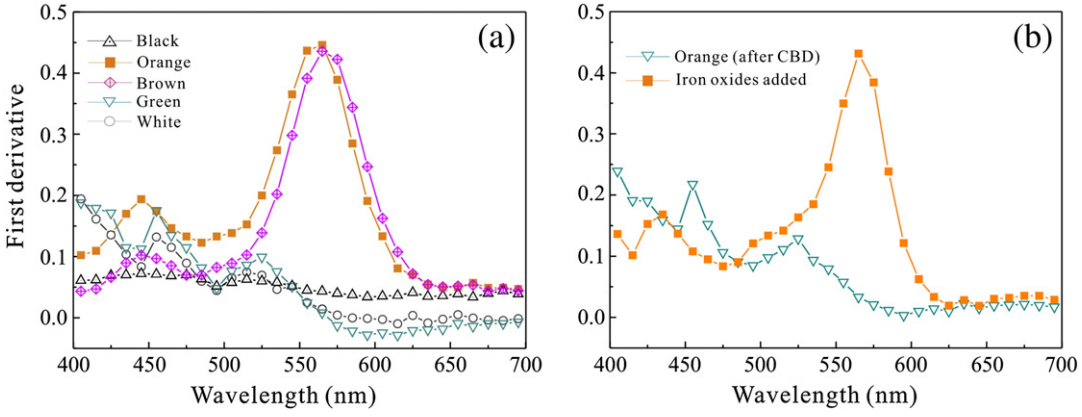

Fig. 3. First derivative spectral patterns for samples from Core 12X in ODP Hole 1049C. (a) First derivative spectral patterns for black, orange, brown, green, and white samples. (b) First derivative spectral patterns for an orange sample treated using the CBD procedure and subsequently iron oxides added.

the samples. After CBD treatment, the samples lost their orange color and became greenish, and no longer yielded peaks at 435 and 565 nm in the first derivative curve (Fig. 3b).

3) Adding iron oxides to matrix materials to create a calibration sample set
Based on CBD extractable iron data and a comparison of the obtained first derivative curves with those described in previous studies (Deaton and Balsam, 1991; Harris and Mix, 1999; Ji et al., 2002), we can estimate the content ranges of hematite and goethite in the red (i.e., brown and orange) samples. Our calibration set consisted of 21 samples (Table 1), obtained by adding known quantities of pigment-grade synthetic hematite and goethite to matrix materials, following Scheinost et al. (1998) and Ji et al. (2002). For the hematite standard, we used Pfizer Inc. R1559, a pure red Fe oxide; for goethite, we used Hoover Color Corp. Synox HY610 Yellow. XRD analyses revealed that both oxides have appropriate crystallography; that is, they are fine-grained (micron- or sub-micro-sized powders), similar to the iron oxides found in deep-sea sediments (Ji et al., 2002). Following addition of the iron oxides, the samples became pale orange, and the hematite and goethite peaks were again observed in the first derivative curves (Fig. 3b).

4) Multiple linear regression
Previous studies have demonstrated the effectiveness of multiple linear regression for spectral characterization of sediment composition (Balsam and Deaton, 1996; Ji et al., 2002). Known contents of hematite/goethite served as dependent variables, while independent variables were spectral violet, blue, green, yellow, orange, and red of calibration samples. Stepwise multiple linear regression was used to establish the calibration equation among hematite/goethite contents and the six spectral bands (Table 1). The choice of variables to include in the regression equation was made by stepwise regression. The results are as follows:

$$\text{Hematite}\ (\%) = 12.022 - 0.590 \times \text{Blue}\ (\%) + 0.165 \times \text{Green}\ (\%) - 0.819 \times \text{Yellow}\ (\%) \quad (1)$$

$$\text{Goethite}\ (\%) = -33.886 + 0.831 \times \text{Green}\ (\%) - 0.455 \times \text{Yellow}\ (\%) + 1.323 \times \text{Orange}\ (\%) \quad (2)$$

Table 1
Hematite and goethite concentrations, and reflectance in various color bands for the calibration sample set.

Sample	Hematite (%)	Goethite (%)	Violet (%)	Blue (%)	Green (%)	Yellow (%)	Orange (%)	Red (%)
1	0.00	0.00	13.39	12.11	23.59	10.74	14.45	25.72
2	0.05	0.10	12.30	11.13	22.43	11.14	15.45	27.56
3	0.00	0.05	13.10	11.89	23.57	10.84	14.61	25.99
4	0.10	0.10	12.03	10.73	21.64	11.22	15.91	28.47
5	0.10	0.20	11.32	10.36	21.54	11.44	16.25	29.09
6	0.20	0.20	10.70	9.63	20.09	11.56	17.13	30.89
7	0.20	0.30	10.59	9.68	20.36	11.58	17.06	30.73
8	0.60	0.40	8.86	7.97	17.15	11.65	19.14	35.23
9	0.30	0.10	10.28	9.04	18.72	11.56	17.89	32.51
10	0.30	0.30	10.10	9.17	19.33	11.63	17.70	32.07
11	0.60	0.20	9.24	8.13	17.18	11.57	18.97	34.90
12	0.40	0.25	9.75	8.75	18.48	11.63	18.20	33.20
13	0.40	0.40	9.48	8.67	18.62	11.71	18.25	33.26
14	0.25	0.50	9.75	9.14	19.80	11.77	17.64	31.89
15	0.25	0.40	10.00	9.26	19.82	11.70	17.52	31.69
16	0.50	0.50	9.02	8.25	17.89	11.73	18.76	34.35
17	0.50	0.60	8.39	7.81	17.41	11.89	19.24	35.25
18	1.00	0.50	7.56	6.77	14.98	11.59	20.57	38.52
19	0.80	0.30	8.64	7.66	16.45	11.59	19.51	36.15
20	0.25	0.80	9.54	9.17	20.32	11.90	17.52	31.55
21	0.30	0.70	9.68	9.12	19.90	11.81	17.64	31.85

4. Results

4.1. Sedimentary cycles

The Aptian–Albian sediments encountered in Core 12X of Hole 1049C are characterized by high-frequency cycles consisting of oceanic red and green/white clayey chalk, and claystone. We divided the sediments within Core 12X into eight cycles of red–white beds, based on color change and magnetic susceptibility (Fig. 2). The thicknesses of the cycles (from top to bottom) were 580, 420, 650, 320, 310, 350, 380, and 330 mm. As shown in Leckie et al.'s (2002) study on biochronology and Huber's (Smithsonian Institution, National Museum of Natural History, personal communication) analysis of fossil foraminifera, the ages of the top (145.3 mbsf) and bottom (150 mbsf) of the *P. eubejaouaenisis* zone are 112.4 and 114.3 Ma, respectively. The corresponding sedimentation rate for the 4.7 m interval between these two boundaries is 2.47 mm/ka. The age of the top of the *G. algerianus* zone (153.2 mbsf) is 115.2 Ma (Bellier et al., 2000), yielding a sedimentation rate of 3.56 mm/ka over the 3.2 m interval from this point to the bottom of the *P. eubejaouaenisis* zone. Given that the top of the *H. rischi* zone is not exposed, we are unable to calculate the sedimentation rate for this interval.

Previous studies of paleomagnetism and astronomical cycles have reported sedimentation rates of 4 mm/ka (250 ky/m) during the Late Aptian and 5.88 mm/ka during the Early Albian (Ogg and Bardot, 2001; Ogg et al., 1999), within an order of magnitude of the rates calculated in the above studies. In this paper, we use Ogg et al.'s (1999) data in calculating the sedimentation rates during the Early Albian and Later Aptian, respectively. Based on these data, combined with the thicknesses of each pair of cyclic red–white beds, we calculated the duration of each cycle, yielding values of (from top to bottom) 99, 71, 111, 54, 53, 88, 95, and 83 ka. The lowest of these values are comparable to the 53.6 ka cycle of the weak obliquity of the Earth's axis, and the highest are comparable to the 85–140 ka cycle of the short eccentricity of Milankovitch cycles.

4.2. Contents of CBD extractable iron

The analysis results of CBD extractable iron reveal that Albian brown beds contain 0.52–1.96% (average value, 1.29%) Fe_2O_3, Aptian orange beds contain 0.41–1.03% (average value, 0.74%) Fe_2O_3. The contents of CBD extractable iron in Albian brown beds are generally higher than those in Aptian orange beds. The contents of CBD extractable iron in cycles 1, 2, 3 are higher than those either in other Albian brown beds or in Aptian orange beds.

4.3. Quantitative XRD analysis

XRD analyses reveal that the samples consist mainly of quartz, albite, and clay minerals. The clay fraction is mainly illite, with subordinate chlorite and minor kaolinite. The contents of quartz show peaks in cycles 1, 3, 4, 8 in the red beds, and the contents of quartz in cycles 2, 7 in the red beds are lower than in the adjacent white beds. The contents of albite in cycles 1 and 7 are higher in the red beds than in the adjacent white beds, and also decrease from the white beds of cycle 3 to red of cycle 2 followed by increasing from red of cycle 2 to red of cycle 1. The contents of illite appear generally higher in the Aptian cycles than in the Albian cycles. However, there are no obvious relationship between the mineral variation patterns and sediment color changes neither in the Albian cycles nor in the Aptian cycles (Fig. 4). We also found that the contents of clay minerals do not show systematic changes with depth, for example, illite and chlorite does replace smectite with increasing burial depth. This indicates that the sediments in ODP Hole 1049C were not influenced by late diagenesis.

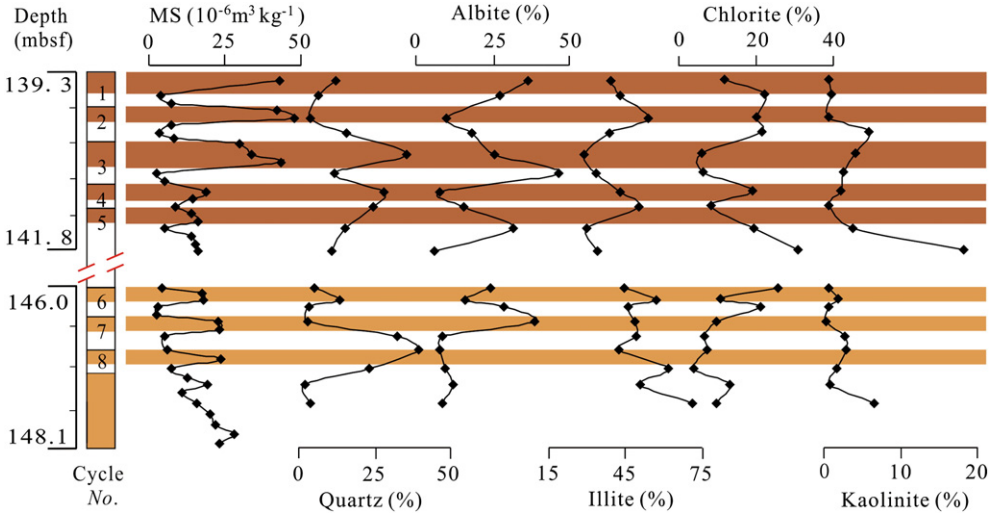

Fig. 4. Comparison of magnetic susceptibility with concentrations of quartz, albite, illite, chlorite, and kaolinite in non-carbonate fraction quantitatively analyzed by Whole Pattern Fitting using software Topas. MS: magnetic susceptibility (data from Han et al., 2008).

4.4. Iron oxide concentrations

Based on the above regression equations, we quantitatively calculated the concentrations of hematite and goethite in the analyzed samples. Albian brown beds contain 0.13–0.82% hematite (average value, 0.51%) and 0.22–0.81% goethite (average value, 0.58%). Aptian orange beds contain 0.19–0.46% hematite (average value, 0.35%) and 0.29–0.67% goethite (average value, 0.50%) (Fig. 5). The hematite and goethite contents in Albian brown beds (cycles 1, 2, and 3) are generally higher than those in Aptian orange beds. The white, green, and black beds contain neither hematite nor goethite. Goethite shows peaks in abundance in some samples adjacent to black beds.

5. Discussion

5.1. Reliability of quantitative estimates of iron oxide concentrations

There are currently two effective methods of detecting low concentrations of hematite and goethite: voltammetric analysis (Grygar and van Oorschot, 2002) and visible light diffuse reflectance spectrophotometry (Balsam and Deaton, 1991; Deaton and Balsam, 1991; Ji et al., 2002; Schwertmann, 1988; Torrent et al., 2006). The detection limits of these methods are about 0.01%. Following the method described by Ji et al. (2002), we obtained two regression equations using diffuse reflectance spectroscopy with multiple linear

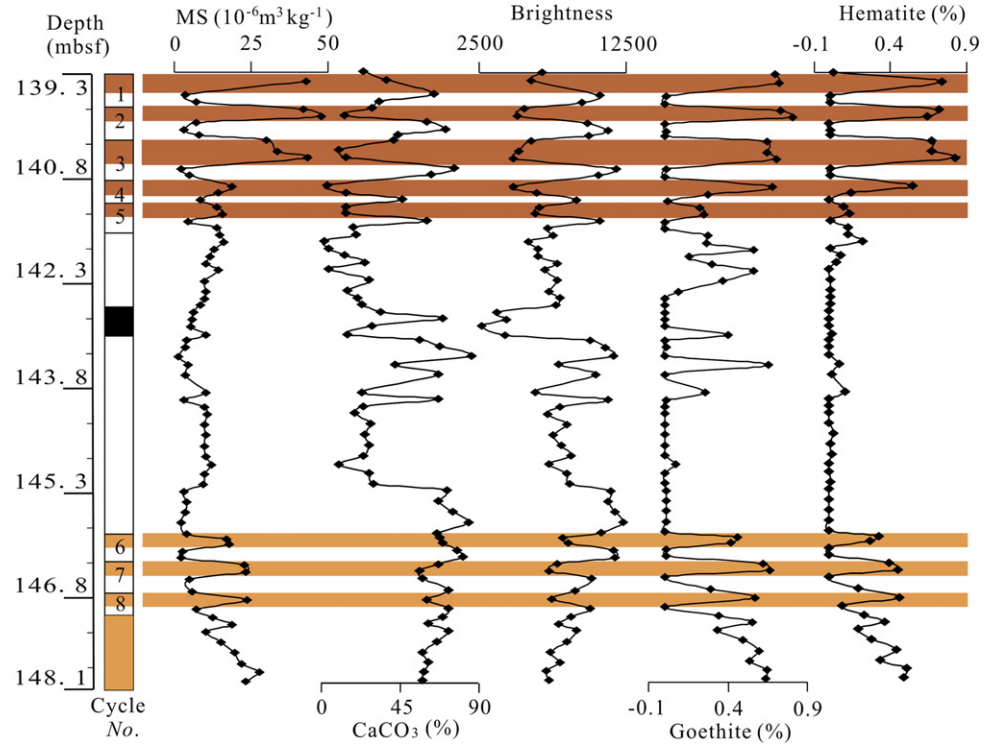

Fig. 5. Comparison of magnetic susceptibility, carbonate content, brightness, goethite content, and hematite content for Core 12X from ODP Hole 1049C (carbonate content data from Han et al., 2008).

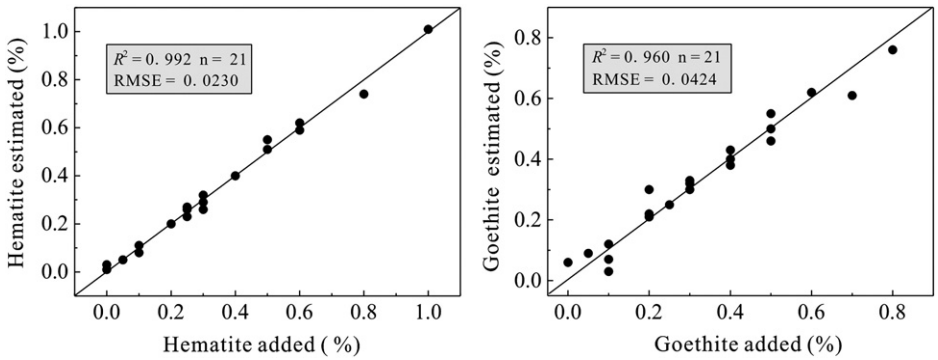

Fig. 6. Comparison of added, known iron oxide contents in the calibration sample set with that estimated by the regression equations. Also showing are the $Y = X$ regression line, the square of the correlation coefficient (R^2), and the root mean square error (RMSE).

regression as mentioned above. In the regression equation for hematite, spectral blue and yellow are negatively correlated with hematite content, whereas spectral green shows a positive correlation. In the regression equation for goethite, spectral yellow shows a negative correlation with goethite content, whereas spectral green and orange show a positive correlation. The hematite and goethite contents estimated from these regression equations lie near the line Y = X (Fig. 6), where X is the added, known content of hematite or goethite, and Y is the hematite or goethite content estimated from the regression equations. For the hematite estimates, R^2 is 0.992, the root mean square error (RMSE) is 0.0230, and the hematite content ranges from 0 to 1.00 wt.%. For the goethite estimates, R^2 and RMSE are 0.960 and 0.0424, respectively, and the goethite content ranges from 0 to 0.80 wt.%. Thus, the calibration equations are satisfactory and the estimated hematite and goethite contents are reliable for contents in the above ranges.

We calculated hematite and goethite contents using the regression equations presented above. The calculated contents correspond well to color changes: orange and brown beds are rich in hematite and goethite, whereas yellow beds adjacent to black beds contain only goethite. White and green beds contain no hematite or goethite (Fig. 5). To assess the accuracy of our quantitative estimates of hematite and goethite content, we compared the obtained values with the concentrations of CBD extractable iron in the red (brown and orange) samples. The CBD extractable iron has been used to estimate the amount of free iron oxides (hydroxides) in sediments. In oceanic sediments it is mainly composed of hematite and goethite with a lesser amount of maghemite and magnetite. Ideally, the estimated hematite plus goethite content will be close to or slightly less than the contents of CBD extractable iron. In this study, our estimates were a little less than the contents of CBD extractable iron in Albian brown samples while our estimates are a little higher than the contents of CBD extractable iron in Aptian orange samples. Nevertheless, there are strong linear relationships between our estimates and the contents of CBD extractable iron (Fig. 7). The R^2 are 0.959 and 0.919 for Albian brown and Aptian orange samples, respectively, demonstrating that our estimates are realistic.

5.2. Controls on sediment color

5.2.1. Red color (brown and orange) samples

Hematite and goethite are ubiquitous in surface environments upon Earth. These minerals are pigments, meaning that they play an important role in determining the color of sediments. Previous studies have shown that the reddish color of sediments is controlled by iron oxides, especially hematite and goethite (Balsam and Deaton, 1991; Balsam et al., 2004; Harris and Mix, 1999; Scheinost et al., 1998). The color of oceanic red beds from ODP 1049C is mainly controlled by hematite and goethite, as supported: (1) the first derivative curves of diffuse reflection show the characteristic peaks of hematite and goethite in brown and orange samples, but not in white, green, or black samples; (2) after treatment using the CBD procedure, the brown and orange samples showed a change in color to greenish or whitish, and the hematite and goethite peaks disappeared from the first derivative curves. Subsequently, after adding varying contents of hematite and goethite to the treated samples, the characteristic peaks re-appeared, and the samples reverted to their original brown and orange colors.

However, hematite and goethite behave differently in terms of determining the color of sediments. Hematite appears blood-red in color (3.5R-4.1YR, Munsell hue), thereby imparting a red color to sediment. In contrast, goethite is bright yellow (8.1YR-1.6Y, Munsell hue), imparting a bright yellow color to sediment (Deaton and Balsam, 1991; Torrent et al., 2006). When hematite alone was added to calibration samples in the present study, the matrix became reddish in color. When goethite alone was added, the matrix became

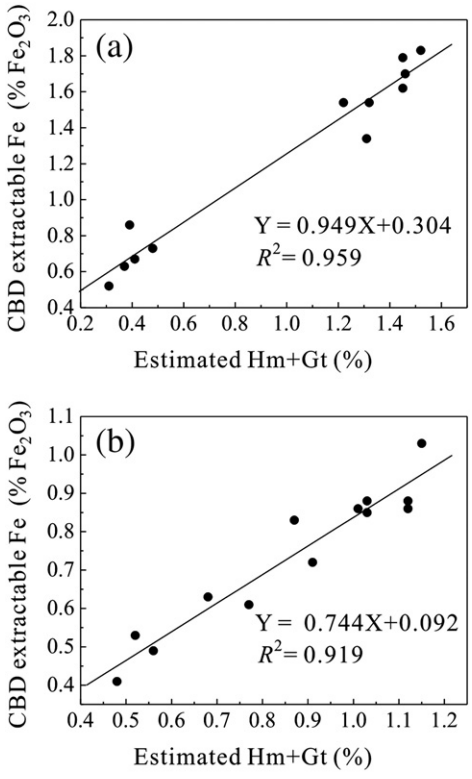

Fig. 7. Combined hematite–goethite concentration versus concentration of CBD extractable iron: (a) for Albian brown samples; (b) for Aptian orange samples.

yellowish. Furthermore, the matrix became orange when we added less than 0.3% hematite combined with more than 0.5% goethite, and it became brown when we added more than 0.5% hematite combined with less than 0.8% goethite. We also found that the red color of hematite has a strong masking effect on the yellow color of goethite, as suggested by Torrent et al. (1983). This finding was supported by our quantitative estimates of the amounts of hematite and goethite: the brown layers contained a higher concentration of hematite (average value, 0.51%) than that of the orange layers (~0.35%), while concentrations of goethite are similar in both brown and orange layers.

It is interesting to note that the Upper Cretaceous red pelagic limestones from central Italy have a characteristic peak of hematite at 565 nm and lack the characteristic peaks of goethite at 435 nm in the first derivative curves of DRS (Hu et al., 2009). The red color of these limestones has been explained by the presence of hematite without goethite (Hu et al., 2009). We propose that goethite in these rocks originally formed together with hematite, but was subsequently transformed to hematite during late diagenesis, based on the observations that 1) the CORBs of central Italy and Blake Nose (North Atlantic) have similar compositions and were deposited in similar pelagic environments, and 2) the red limestones in Italy are lithified and experienced considerable diagenesis (Arthur and Fischer, 1977), whereas the red marls in Hole 1049C are largely unaffected by diagenesis (Erbacher et al., 2001). The importance of the goethite–hematite transition in red beds has also been emphasized in previous studies (Channell et al., 1982; Gualtieri and Venturelli, 1999).

5.2.2. Green and white samples

The green samples contain no iron oxides. The color of these samples is possibly controlled by Fe^{2+}-bearing silicate clay minerals (chlorite), as a high value of Fe^{2+}/Fe^{3+} in the crystal structure of silicate clay minerals can impart a green color to sediments (Giosan et al., 2002a, 2002b; Lyle, 1983). In an analysis of chlorite, Ji et al. (2006) reported two distinct absorption peaks of iron in the spectral region between 800 and 1400 nm: one centered near 930 nm, due to Fe^{3+} in six-fold coordination, and one centered at 1140 nm, due to Fe^{2+} in six-fold coordination. Because the peak depth in a continuum-removed reflectance spectrum provides information on the mineral content of sediments (Clark and Roush, 1984), it is useful to calculate the ratio of the 1140 nm absorption peak depth to the 930 nm absorption peak depth. This ratio represents the value of Fe^{2+}/Fe^{3+} in clay minerals. The green sample in our study shows these two peaks (Fig. 8), and the peak depth of Fe^{2+} clearly exceeds that for Fe^{3+}. Thus, the green color of the sample may reflect a high proportion of Fe^{2+} (or high value of Fe^{2+}/Fe^{3+}) in the chlorite structure. In fact, the orange samples do not show the two characteristic peaks of chlorite in DRS curves. However, in the case that iron oxides are removed from the orange sample using the CBD procedure, the 930 and 1140 nm peaks appear, and the sample color changes to green (Fig. 8). This finding indicates that orange samples contain chlorite, although not enough to generate its two peaks in reflectance spectra, due to the masking effect of iron oxides (see Balsam and Deaton, 1991; Giosan et al., 2002a).

The white samples contain a high concentration of calcium carbonate (average value, 69.5%; Han et al., 2008) and minor chlorite (less than 5%). The reflection spectrum obtained for white samples does not show the characteristic peaks for hematite or goethite, and it is difficult to identify the absorption peak of chlorite. The low concentration of chlorite indicates that it has negligible influence on the color of white samples (Fig. 8). Therefore, the color of white samples mainly reflects the high content of calcium carbonate.

5.3. Factors influencing the formation of oceanic red beds

5.3.1. Terrigenous input

XRD analyses reveal that the terrigenous components in the samples are mainly quartz, albite, and clay minerals. The clay fraction is mainly illite and chlorite, with minor kaolinite. This clay assemblage is typical of a dry and cold climate, with little rainfall in the source area. In such environments, weathering occurs mainly via physical processes or weak chemical processes, with little eluviation (Gingele et al., 2001; Winkler et al., 2002).

In the cycles considered in the present study, the content ranges of quartz, albite, clay minerals (e.g., illite, chlorite, and kaolinite) in the sediments of Albian cycles and Aptian cycles are not obviously different with depth. Apart from the magnetic susceptibility there are also not obvious variations of mineral contents with sediment color, neither in the Albian cycles nor in the Aptian cycles. The contents of quartz and albite show similar variations in cycles 1, 2, 3 while illite has the opposite variation pattern in the same cycles. It seems that the minerals may follow a lower frequent cyclicity, possibly spanning 2 or 3 color cycles. The mineral variation and color changes might be related to climate variability, but obviously on different cyclicities. A previous chemical analysis of the same core (Cheng, 2008) revealed strong positive correlations among Si, Al, Mg, Fe, Na, K, and Ti, which represent terrestrial input, thereby providing further evidence of a consistent source area during deposition of the sediments.

5.3.2. Paleoceanographic conditions

The stability of terrigenous input described above suggests that iron oxides, which are responsible for change in sediment color, were

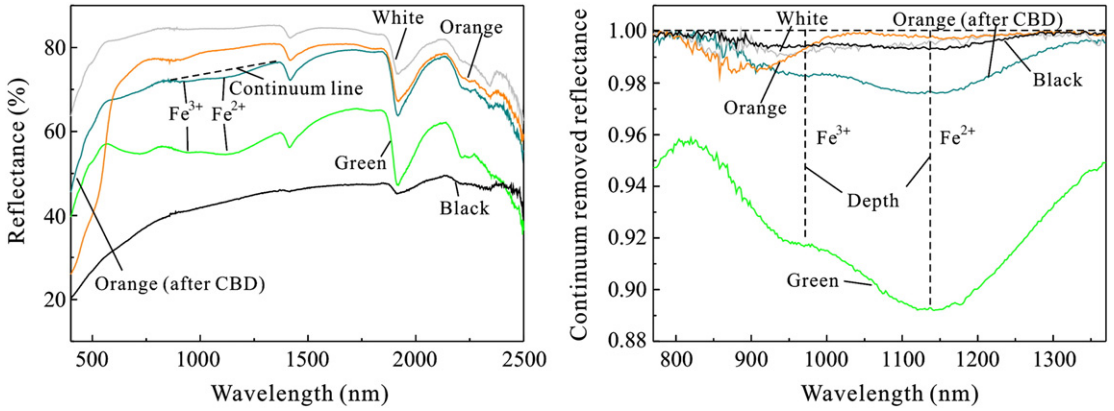

Fig. 8. Diffuse reflectance spectra (left) and continuum-removed reflectance spectra (right) of samples colored black, green, white, and orange. Also shown for comparison is a CBD-treated orange sample. The continuum-removal approach involved fitting a straight line to the reflectance continuum using two continuum tie points, on either side of the absorption feature (Clark and Roush, 1984).

derived from syn-depositional oxidation and influenced by early diagenesis rather than terrigenous clastics. The hematite and goethite in brown and orange beds may represent oxic bottom conditions at the time of their formation. The hematite and goethite contents of Albian brown beds (average values, 0.51% and 0.58%, respectively) are higher than those of orange beds (average values, 0.35% and 0.50%, respectively), indicating relatively oxic bottom conditions during the Albian. Trace element analyses of samples from Core 12X (see Cheng, 2008) also support an oxic environment during the deposition of brown and orange beds. In the brown, orange, white, and black beds, trace elements such as V, Co, Ni, U, and Cu, which are sensitive to redox conditions, are depleted, depleted to weakly enriched, weakly enriched, and highly enriched, respectively.

Which factors caused the postulated fluctuations in redox conditions? Morford and Emerson (1999) reported that the joint effects of the accumulation rate of organic matter and dissolved oxygen content in bottom waters directly determine the redox condition at the sediment–water interface. Dissolved oxygen in bottom waters acts as an oxidant, while organic matter acts as a reducer. We speculate that the oxic environment recorded by Aptian–Albian red beds resulted from either a high content of dissolved oxygen or low accumulation rate of organic material. MacLeod et al. (2001) investigated planktonic foraminifera and whole-rock stable isotopes in Maastrichtian sediments from ODP Hole 1050C (adjacent to the Hole 1049C of this study), and concluded that reddish layers resulted from low primary productivity. However, existing data on the studied samples from ODP 1049C do not enable us to calculate the dissolved oxygen contents or accumulation rate of organic matter; consequently, additional work is required in this regard.

The occurrence of iron oxides in the sediments can be also influenced by early diagenetic processes. As mentioned above, planktonic and benthic species have glassy shells with preserved surface ornamentation and lack infilling calcite which indicates that the sediments are unconsolidated and did not undergo strongly compaction. This may lead the sediments to retain higher sediment porosity and higher oxygen exposure time, which determines the flux of oxygen into the pore water. In the early diagenetic processes, high oxygen content in the pore water will favor the final appearance of iron oxides in the red sediments when the accumulation rate of organic matter is at a low level.

6. Conclusions

(1) Visible light diffuse reflectance spectrophotometry proved to be a rapid and precise method of quantifying the absolute concentrations of hematite and goethite in sediments from Core 12X, ODP Hole 1049C, North Atlantic. The hematite and goethite contents obtained using this method have been demonstrated to be reliable.

(2) A quantitative analysis of iron oxide contents within Core 12X reveals that Albian brown beds contain 0.13–0.82% hematite (average value, 0.51%) and 0.22–0.81% goethite (average value, 0.58%). Aptian orange beds contain 0.19–0.46% hematite (average value, 0.35%) and 0.29–0.67% goethite (average value, 0.50%).

(3) Hematite and goethite are responsible for the reddish color of the examined samples. However, these minerals behave differently in terms of determining the color of sediment: hematite imparts a red color to sediment whereas goethite imparts a yellow color. A change in the proportions of these minerals can cause a change in sediment color from orange to brown.

(4) Hematite and goethite within the red beds formed in an oxic environment during the period of deposition and early diagenesis. The oxic conditions were probably determined by the low accumulation rate of organic matter and the high content of dissolved oxygen in bottom water.

Acknowledgements

Samples analyzed in this study were provided by the Ocean Drilling Program. We thank Mr. Wenbin Cheng for providing geochemical data, and B. Huber for making available unpublished data and for many helpful discussions. We also thank Prof. Junfeng Ji for assistance with DRS. This paper benefited from the constructive reviews by Dr. Ines Wendler and Prof. Michael Wagreich. This study was financially supported by the MOST 973 Project (2006CB701402) and an NSFC Project (40625012). This is a contribution to the IGCP555.

References

Arthur, M.A., Fischer, A.G., 1977. Upper Cretaceous–Paleocene magnetic stratigraphy at Gubbio, Italy I. Lithostratigraphy and sedimentology.Geological Society of America Bulletin 88, Geological Society of America Bulletin, pp. 367–371.

Balsam, W.L., Damuth, J.E., 2000. Further investigations of shipboard vs. shore-based spectral data: implications for interpreting Leg 164 sediment composition. In: Paull, C.K., Matsumoto, R., Wallace, P.J., Dillon, W.P. (Eds.), Proceedings of Ocean Drilling Program, Scientific Results 164. Ocean Drilling Program, Texas A & M University, College Station, TX, pp. 313–324.

Balsam, W.L., Deaton, B.C., 1991. Sediment dispersal in the Atlantic Ocean: evaluation by visible light spectra. Reviews in Aquatic Sciences 4, 411–447.

Balsam, W.L., Deaton, B.C., 1996. Determining the composition of late Quaternary marine sediments from NUV, VIS and NIR diffuse reflectance spectra. Marine Geology 134, 31–55.

Balsam, W.L., Wolhart, R., 1993. Sediment dispersal in the Argentine Basin: evidence from visible light spectra. Deep-Sea Research 40, 1001–1031.

Balsam, W.L., Deaton, B.C., Damuth, J.E., 1999. Evaluating optical lightness as a proxy for carbonate content in marine sediment cores. Marine Geology 161, 141–153.

Balsam, W.L., Ji, J.F., Chen, J., 2004. Climatic interpretation of the Luochuan and Lingtai loess sections, China, based on changing iron oxide mineralogy and magnetic susceptibility. Earth and Planetary Science Letters 223, 335–348.

Barranco, F., Balsam, W.L., Deaton, B.C., 1989. Quantitative reassessment of brick red lutites: evidence from reflectance spectrophotometry. Marine Geology 89, 299–314.

Bellier, J.P., Moullade, M., Huber, B.T., 2000. Mid-Cretaceous planktonic foraminifers from Blake Nose: revised biostratigraphic framework. In: Kroon, D., Norris, R.D., Klaus, A. (Eds.), Proceedings of the Ocean Drilling Program: Scientific Results 171B. College Station, TX (Ocean Drilling Program), pp. 1–12.

Benson, W.E., Sheridan, R.E., Enos, P., Freeman, T., Gradstein, F., Murdmaa, I.O., Pastouret, L., Schmidt, R.R., Stuermer, D.H., Weaver, F.M., Worstell, P., 1978. Sites 389 and 390: north rim of Blake Nose (Shipboard Scientific Party). In: Benson, W.E., Sheridan, R.E., Enos, P., Freeman, T., Gradstein, F., Murdmaa, I.O., Pastouret, L., Schmidt, R.R., Stuermer, D.H., Weaver, F.M., Worstell, P. (Eds.), Initial Reports of the Deep Sea Drilling Project 44. U.S. Government Printing Office, Washington, pp. 69–151.

Channell, J.E.T., Freeman, R., Heller, F., Lowrie, W., 1982. Timing of diagenetic hematite growth in red pelagic limestones from Gubbio (Italy). Earth and Planetary Science Letters 58, 189–201.

Chen, X., Wang, C.S., Hu, X.M., Huang, Y.J., Wang, P.K., Jansa, L., Zeng, X., 2007. Cretaceous oceanic red beds: distribution, lithostratigraphy and paleoenvironments. Acta Geologica Sinica (English Edition) 81, 1070–1086.

Cheng, W.B., 2008. Element geochemical record of Cretaceous oceanic red beds: implications for paleoceanic environment. Master's thesis. China University of Geosciences (Beijing), Beijing, China.

Clark, R.N., Roush, T.L., 1984. Reflectance spectroscopy: quantitative analysis techniques for remote sensing applications. Journal of Geophysical Research 89, 6329–6340.

Deaton, B.C., Balsam, W.L., 1991. Visible spectroscopy—a rapid method for determining hematite and goethite concentration in geological materials. Journal of Sedimentary Petrology 61, 628–632.

Erbacher, J., Huber, B.T., Norris, R.D., Markey, M., 2001. Increased thermohaline stratification as a possible cause for an ocean anoxic event in the Cretaceous period. Nature 409, 325–327.

Eren, M., Kadir, S., 2001. Color genesis of Upper Cretaceous pelagic red sediments within the Eastern Pontides, NE Turkey, Yerbilimleri 24, pp. 71–79.

Gingele, F.X., Deckker, P.De., Hillenbrand, C.D., 2001. Late Quaternary fluctuations of the Leeuwin Current and palaeoclimates on the adjacent land masses: clay mineral evidence. Australian Journal of Earth Sciences 48, 867–874.

Giosan, L., Flood, R.D., Aller, R.C., 2002a. Paleoceanographic significance of sediment color on western North Atlantic drifts: I. Origin of color. Marine Geology 189, 25–41.

Giosan, L., Flood, R.D., Grutzner, J., Mudie, P., 2002b. Paleoceanographic significance of sediment color on western North Atlantic drifts: II. Plio-Pleistocene sedimentation. Marine Geology 189, 43–61.

Grygar, T., van Oorschot, I.H.M., 2002. Voltammetric identification of pedogenic iron oxides in paleosol and loess. Electroanalysis 14, 339–344.

Gualtieri, A.F., Venturelli, P., 1999. In situ study of the goethite-hematite phase transformation by real time synchrotron powder diffraction. American Mineralogist 84, 895–904.

Han, Z.Y., Hu, X.M., Ji, J.F., Huang, Y.J., Huang, Z.C., 2008. Origin of the Aptian–Albian high cyclic oceanic red beds in the ODP Hole 1049C, North Atlantic: mineralogical evidence. Acta Geologica Sinica 82, 124–132.
Harris, S.E., Mix, A.C., 1999. Pleistocene precipitation balance in the Amazon Basin recorded in deep sea sediments. Quaternary Research 51, 14–26.
Hu, X.M., Jansa, L., Wang, C.S., Sarti, M., Bak, K., Wagreich, M., Michalik, J., Sotak, J., 2005. Upper Cretaceous oceanic red beds (CORBs) in the Tethys: occurrences, lithofacies, age and environments. Cretaceous Research 26, 3–20.
Hu, X.M., Jansa, L., Sarti, M., 2006a. Mid-Cretaceous oceanic red beds in the Umbria-Marche Basin, central Italy: constraints on paleoceanography and palaeoclimate. Palaeogeography, Palaeoclimate, Palaeoecology 233, 163–186.
Hu, X.M., Wang, C.S., Li, X.H., Jansa, L., 2006b. Upper Cretaceous oceanic red beds in southern Tibet: lithofacies, environments and colour origin. Science in China Series D-Earth Sciences 49, 785–795.
Hu, X.M., Cheng, W.B., Ji, J.F., 2009. Origin of Cretaceous oceanic red beds from the Vispi Quarry section, central Italy: visible reflectance and inorganic geochemistry. In: Hu, X.M., Wang, C.S., Scott, R.W., Wagreich, M., Jansa, L. (Eds.), Cretaceous Oceanic Red Beds: Stratigraphy, composition, origins and paleoceanographic and paleoclimatic significance. SEPM Special Publication 91, 183–197.
Ji, J.F., Balsam, W.L., Chen, J., Liu, L.W., 2002. Rapid and quantitative measurement of hematite and goethite in the Chinese loess-paleosol sequence by diffuse reflectance spectroscopy. Clays and Clay Minerals 50, 208–216.
Ji, J.F., Zhao, L., Balsam, W.L., Chen, J., Wu, T., Liu, L.W., 2006. Detecting chlorite in the Chinese loess sequence by diffuse reflectance spectroscopy. Clays and Clay Minerals 54, 266–273.
Judd, D.B., Wyszecki, G., 1975. Color in business, science, and industry. Wiley, New York.
Klaus, A., Norris, R.D., Kroon, D., Smit, J., 2000. Impact-induced K–T boundary mass wasting across the Blake Nose, western North Atlantic. Geology 28, 319–322.
Leckie, R.M., Bralower, T.J., Cashman, R., 2002. Oceanic anoxic events and plankton evolution: biotic response to tectonic forcing during the mid-Cretaceous. Paleoceanography 17, 1–29.
Lyle, M., 1983. The brown-green color transition in marine sediments: a marker of the Fe (III)-Fe (II) redox boundary. Limnology and Oceanography 28, 1026–1033.
MacLeod, K.G., Huber, B.T., Pletsch, T., RÖhl, U., Kucera, M., 2001. Maastrichtian foraminiferal and paleoceanographic changes on Milankovitch timescales. Paleoceanography 16, 133–154.
Mehra, O.P., Jackson, M.L., 1960. Iron oxide removal from soils and clays by a dithionate-citrate system buffered with sodium bicarbonate. Clays and Clay Minerals 7, 317–327.
Melinte, M.C., Jipa, D., 2005. Campanian–Maastrichtian marine red beds in Romania: biostratigraphic and genetic significance. Cretaceous Research 26, 49–56.
Morford, J.L., Emerson, S., 1999. The geochemistry of redox sensitive trace metals in sediments. Geochimica Cosmochimica Acta 63, l735–1750.
Neuhuber, S., Wagreich, M., Wendler, I., Spotl, C., 2007. Turonian oceanic red beds in the eastern Alps: concepts for palaeoceanographic changes in the Mediterranean Tethys. Palaeogeography, Palaeoclimatology, Palaeoecology 251, 222–238.
Norris, R.D., Kroon, D., Klaus, A., et al., 1998. Shipboard Scientific Party. In: Norris, R.D., Kroon, D., Klaus, A., et al. (Eds.), Proceedings of the Ocean Drilling Program. Initial Reports 171B, College Station, TX. Ocean Drilling Program.
Norris, R.D., Kroon, D., Huber, B.T., Erbacher, J., 2001. Cretaceous–Paleogene ocean and climate change in the subtropical North Atlantic. In: Kroon, D., Norris, R.D., Klaus, A. (Eds.), Western North Atlantic Palaeogene and Cretaceous Palaeoceanography, 183. Geological Society of London, Special Publications, London, pp. 1–22.
Ogg, J.G., Bardot, L., 2001. Aptian through Eocene magnetostratigraphic correlation of the Blake Nose Transect (Leg 171B), Florida continental margin. In: Kroon, D., Norris, R.D., Klaus, A. (Eds.), Proceedings of the Ocean Drilling Program: Scientific Results 171B. College Station, TX (Ocean Drilling Program), pp. 1–58.
Ogg, J.G., Röhl, U., Geib, T., 1999. Astronomical tuning of Aptian–Albian boundary interval: oceanic anoxic event 1b through lower Albian magnetic suchron M″-2″r. Eos 80, F491–F492.
Premoli-Silva, I., Caron, M., Leckie, R.M., Petrizzo, M.R., Soldan, D., Verga, D., 2009. *Paraticinella* n. gen. and taxonomic revision of *Ticinella bejaouaensis* Sigal, 1966. Journal of Foraminiferal Research 29 (2), 126–137.
Scheinost, A.C., Chavernas, A., Barrón, V., Torrent, J., 1998. Use and limitations of second-derivative diffuse reflectance spectroscopy in the visible to near-infrared range to identify and quantify Fe oxide minerals in soils. Clays and Clay Minerals 46, 528–536.
Schwertmann, U., 1988. Occurrence and formation of iron oxides in various pedoenvironments. In: Stucki, J.W., Goodman, B.A., Schwertmann, U. (Eds.), Iron in soils and clay minerals., C 127. D Reidel Publishing Company, NATO ASI Series, pp. 267–308.
Skelton, P.W., Spicer, R.A., Kelley, S.P., Gilmour, I., 2003. The Cretaceous world. Cambridge University Press, London.
Tarduno, J.A., Brinkman, D.B., Renne, P.R., Cottrell, R.D., Scher, H., Castillo, P., 1998. Evidence for extreme climatic warmth from Late Cretaceous Arctic vertebrates. Science 282, 2241–2244.
Torrent, J., Schwertmann, U., Fechter, H., Alferez, F., 1983. Quantitative relationships between soil color and hematite content. Soil Science 136, 354–358.
Torrent, J., Barrón, V., Liu, Q., 2006. Magnetic enhancement is linked to and precedes hematite formation in aerobic soil. Geophysical Research Letters 33, L02401–L02404.
Wagreich, M., Krenmayr, H.-G., 2005. Upper Cretaceous oceanic red beds (CORB) in the Northern Calcareous Alps (Nierental Formation, Austria): slope topography and clastic input as primary controlling factors. Cretaceous Research 26, 57–64.
Wang, C.S., Hu, X.M., Sarti, M., Scott, R.W., Li, X.H., 2005. Upper Cretaceous oceanic red beds in southern Tibet: a major change from anoxic to oxic condition. Cretaceous Research 26, 21–32.
Wang, C.S., Hu, X.M., Huang, Y.J., Scott, R.W., Wagreich, M., 2009. Overview of Cretaceous Oceanic Red Beds (CORBs): a window on global oceanic and climate change. In: Hu, X.M., Wang, C.S., Scott, R.W., Wagreich, M., Jansa, L. (Eds.), Cretaceous Oceanic Red Beds: stratigraphy, composition, origins and paleoceanographic and paleoclimatic significance 91. SEPM Special Publication, pp. 13–33.
Winkler, A., Wolf-Welling, T.C.W., Stattegger, K., Thiede, J., 2002. Clay mineral sedimentation in high northern latitude deep-sea basins since the Middle Miocene (ODP Leg 151, NAAG). International Journal of Earth Sciences 91, 133–148.
Yilmaz, İ.Ö., 2008. Cretaceous pelagic red beds and black shales (Aptian-Santonian), NW Turkey: Global oceanic anoxic and oxic events. Turkish Journal of Earth Sciences 17, 263–296.